# We are IntechOpen,
# the world's leading publisher of
# Open Access books
# Built by scientists, for scientists

## 4,800
Open access books available

## 122,000
International authors and editors

## 135M
Downloads

Our authors are among the

## 154
Countries delivered to

## TOP 1%
most cited scientists

## 12.2%
Contributors from top 500 universities

**BOOK CITATION INDEX**
CLARIVATE ANALYTICS
INDEXED

**WEB OF SCIENCE™**

Selection of our books indexed in the Book Citation Index
in Web of Science™ Core Collection (BKCI)

## Interested in publishing with us?
## Contact book.department@intechopen.com

Numbers displayed above are based on latest data collected.
For more information visit www.intechopen.com

# Acoustics and Vibro-Acoustics Applied in Space Industry

Rogério Pirk, Carlos d´Andrade Souto,
Gustavo Paulinelli Guimarães and Luiz Carlos Sandoval Góes

Additional information is available at the end of the chapter

## 1. Introduction

During flight, Expandable Launch Vehicles (ELV) are excited by severe acoustic loads in three phases of flight: lift off, transonic flight and maximum dynamic pressure instant [1]. As such, principles to make onboard equipment compatible with the mission environments must be adopted. At lift off, the highly intense acoustic loads occur; and these levels are usually adopted to qualify payloads and equipments. However, during the transonic flight and maximum dynamic pressure phase, acoustic excitation is also present and such characteristics are also significant for performance evaluation as well as for specific system dynamic qualification/acceptance programs. In this way, noise control treatments (NCT) shall be adopted to alleviate internal vibro-acoustic environments, in view of decreasing costs and developments.

The hostile in-flight environments can damage sensors/conditioners as well as make measurements unreliable. In this way, installation adapters must be designed to protect the sensors. The acoustics of such protective cavities influence the measured sound pressure level (SPL) As such, the cavities must be analyzed and their amplitude-frequency characteristics evaluated. Finally, the measurement corrections, necessary to obtain the actual external SPL, are determined.

Concerning the internal environment found during flights, important launcher subsystems as payload fairing (PLF) and equipment bays shall be investigated and vibro-acoustic analysis can be done, as pointed by [2], [3] and [4]. The PLF is the structural compartment of a launcher where the payload is placed during the flight mission. PLF inner acoustics and its attenuation designs, using virtual prototypes are analyzed using deterministic and statistic techniques. However, when in-flight loading are not characterized, the accounted external air-borne excitation can be those described in [5]. In a similar way, SPL along the launcher structure at

lift-off can also be estimated [6]. Furthermore, an alternative procedure to characterize external SPL during flight can also be adopted as described by [7]. Passive vibration control techniques can be used to attenuate structure-borne vibration and the use of viscoelastic materials adding structural damping to reduce the magnitude of vibrations is a well-known solution, usually applied in space and aeronautical industries. On the other hand, the use of active vibration control (AVC) is still considered difficult to be implemented in space industry.

For acoustic noise attenuation, the standard practice is to use passive techniques like blankets ([8] and [9]), which attenuate sound by trapping the energy in the blanket material and dissipating it as heat [10] and Helmholtz resonators tuned to absorb acoustic energy at one or some specific frequencies, typically the cavity frequencies as done by [11].

Another acoustic crucial subject in space industry is combustion instability, since it can severely impair the operation of Liquid Propelled Rocket Engine (LPRE) [12]. In this way, solutions for instability problems in combustion chambers of LPRE as well as solid rocket motors (SRM) are of large interest. In [13], it is described that combustion instability can be verified when the power spectrum of the acoustic pressure measured during tests is analyzed. When an oscillation is observed, i.e., combustion instability, well-defined sound pressure peaks, summed to the background noise are present. Such peaks are correlated to the resonance frequencies of the combustion chamber. In this way, the coupling of acoustic natural frequencies and burning oscillations of the combustion chamber occurs, which can cause instabilities and consequent unexpected behavior as efficiency loss or even the explosion of the engine. In the early developing phases of liquid rocket engines, it is usually proposed the investigation of different combustion chamber configurations [14]. This is usually done in two steps as follows: using theoretical calculation and through experimental measurements. In this way, theoretical and experimental natural frequencies of the acoustic cavity are obtained. Further studies must be performed, applying devices and techniques to attenuate pressure oscillations inside combustion chambers and devices as Helmholtz Resonators, baffles and ¼ wave filters are largely used ([15] and [16]).

This chapter describes three case studies applied on space industry. Firstly, analytical and numerical modelings of in-flight external microphone protection devices are described. Testing procedures and the SPL measurement correction factors determination are also presented. As a second case study, deterministic and statistical coupled vibro-acoustic analysis techniques are used to estimate PLF internal SPL at lift-off as well as to assess the effect of including NCT (blanket materials) on its skin. The modeling procedures and experimental ground test are described. Finally, in the third case, the acoustic characterization of combustion chambers is presented. Cold tests are described as well as the theoretical modeling procedures. The pressure attenuation control technique using Helmholtz Resonators are also presented. In all three case studies, theoretical x experimental results are depicted.

## 2. External on board microphones installation devices

At lift off, the source of the acoustic noise is the gas stream ejected by the motors (Fig. 1). Such acoustic pressure lies in the range of 140 to 180 dB near the rocket and is very close to

an acoustic diffuse field (ADF) noise. At transonic flight the launcher is excited by the turbulent boundary layer (TBL) in the neighborhood of the shock waves. According to [17], when the maximum dynamic pressure occurs, the unsteady pressure field applied to the launcher is due to aerodynamic noise. The characteristics of such noise are very different from those at lift off. Non-attached flows increase the pressure in low-frequencies, which excite the launcher first structural modes. A simulation of the VLS-1 flight aerodynamics was done by Academician V. P. Makeyev State Rocket Centre (SRC- Makeyev), as shown in Fig. 2. Notice that the upper nose and 1st stage noses are the most exposed regions to aero-acoustic noise.
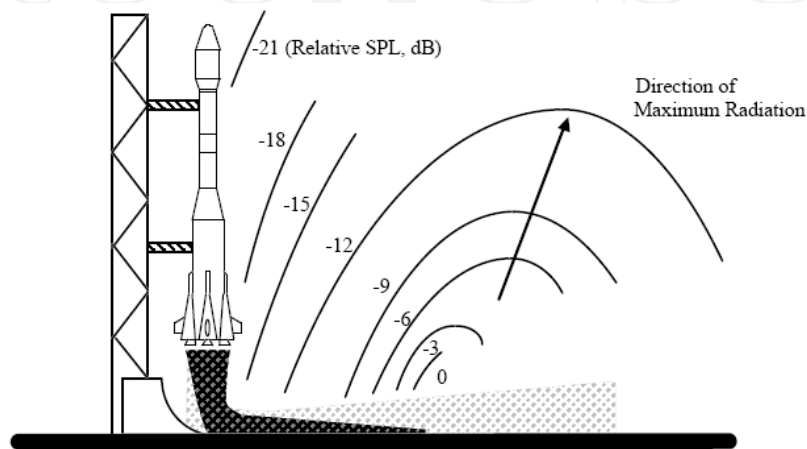
**Figure 1.** Acoustic noise at lift off
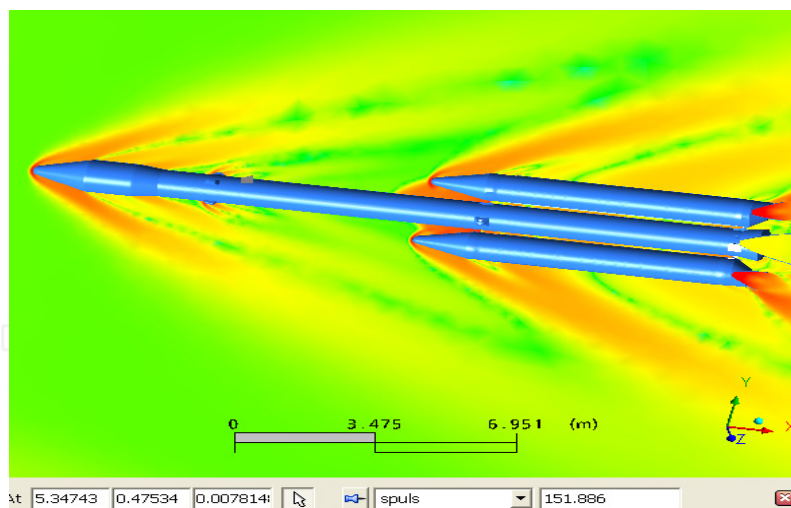
**Figure 2.** In-flight aero-acoustic noise

In view of having a good characterization of the in-flight acoustic loads acting upon the launcher structure, external acoustic measurements are required. Due to the high SPL and hostile environments found during flight, special microphones and adapters are specified. Such adapters must be designed in order to provide appropriate microphone/pre-amplifier installation and protection. Besides, when necessary, measurement correction procedures must be adopted. In this way, measurement programs for in-flight external acoustic

characterization shall be developed, which may take into account three main phases as: preparation for experimental studies and acoustic testing sensors, ground development testing of acoustic sensors and methodology for reading acoustic pressures during flight.

Three different adapters for ¼'' microphones were conceived, as described by [18]. On the upper parts of the launcher, two different configurations can be adopted. Firstly, at the PLF, heating and propellant dust effects are not significant; therefore, a structure flush installation (Fig. 3a) can be used. In this case, the measured SPL can be read directly. The second configuration, straight adapter (Fig. 3b), is applied for microphones installed near the equipment bays, where one has temperature and dust influences and, therefore, the sensor/conditioner must be protected. For such an assemblage, the protection channel dynamics directly affect the sensor response and, as a result, a measurement correction must be done.

On the bottom, the intense SPL at lift off generate a severe acoustic excitation of the first stage back modules region. Highly hostile dust, hot gas flow, heat flux and temperature environments are present during the motors operations. Nevertheless, the angular adapter must be used to install acoustic microphone/pre-amplifier, as shown in Fig. 3c. Notice in Figs. 3b and 3c, that the adapters were designed with small acoustic straight and angular cavities, respectively. When acoustically excited, the acoustical responses of such cavities directly influence the measured SPL, since the external pressure excitation profile and the measured signal are related by the cavity transfer function.



(a)                          (b)                          (c)
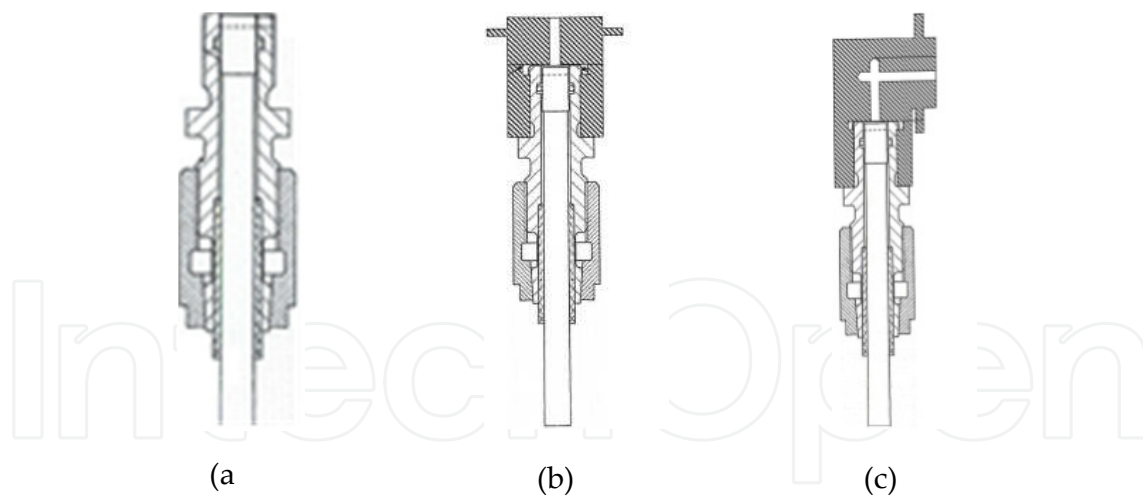
**Figure 3.** (a) Flush adapter; (b) Straight adapter; (c) Angular adapter

In order to determine straight and angular adapters' dynamics, analytical and numerical calculations are done. The transfer functions of these channels are evaluated during ground acoustic tests, on which acoustic excitation with SPL close to those expected during flight is used to excite the cavities. Consequently, the measured SPL as well as the channels transfer functions are determined. Finally, the measurement corrections are determined, which may be applied when these adapters are used.

## 2.1. Mathematical models

### 2.1.1. Analytical model

In view of describing the dynamical behavior of the protective channels, one can assume the straight and angular channels as Helmholtz Resonators, which the channels and the space for microphone installation are accounted as the resonator throat and volume, as described by Eq. (1) [19].

$$f_0 = \frac{c_0}{2\pi}\sqrt{\frac{S}{V_0(l+l_c)}} \tag{1}$$

where: $f_0$ : natural frequency, $c_0$ : sound speed, $S$ : cross section of the resonator throat, $V_0$ : volume of the resonator cavity, $l$ : length of the resonator throat, $l_c = 0.8r$ : end correction and $r$ : radius of the resonator throat cross section.

By considering the dimensions of the adapters into Eq. (1), one can calculate the natural frequencies of the straight and angular channels shown in Figs. 3b and 3c. These calculations are the starting point to assess the accuracy of the numerical models, built by using the Finite Element Method, once analytical x numerical natural frequencies can be compared.

### 2.1.2. Numerical model by Finite Element Method (FEM)

In a similar way as in structural dynamics, an acoustic cavity FEM model will have an acoustic stiffness matrix $[K_a]$, an acoustic mass matrix $[M_a]$, acoustic excitation vectors $\{F_{ai}\}$ and an acoustic damping matrix $[C_a]$. The combination of these components yields the acoustic finite element model, which can be solved for the unknown nodal pressure values $p_i$ [20].

$$\left([K_a] + j\omega[C_a] - \omega^2[M_a]\right).\{p_i\} = \{F_{ai}\} \tag{2}$$

Acoustic finite element models of the three adapters cavities are built. All cavities' surfaces were considered as rigid walls but the openings that are in direct contact with the external acoustic environment. In such cases, opened surfaces approximated using prescribed nodal pressures (equal to 0 for the eigenanalysis) were considered. The fluid inside the cavities is assumed as air at 15° C (c=340 m/s, ϱ=1.225 Kg/m³, values used in this entire chapter).

Linear tetrahedral fluid elements are used in all three meshes. In order to have good prediction accuracy in the frequency range of interest, the general rule of thumb that requires at least 6 elements per wavelength is adopted. The main meshing characteristics are described in Table 1.

The acoustic load generated at lift off is simulated as an acoustic diffuse field (ADF). According to [21], an ADF is defined as an acoustic field in which the SPL is equal at any location and have an identical energy distribution in all directions. Such ADF can be

obtained in an acoustic reverberant chamber, where the reflections along the rigid walls lead to this field. A formal way to describe an ADF consists on superimposing an infinite number of uncorrelated plane waves through different directions. In a FEM model, a finite number of uncorrelated plane waves can be generated and the pressure due the superposition of all the uncorrelated plane waves can then be applied as prescribed nodal pressures on the cavity's open surface (see [22]).

| Parameters | Mesh | | |
| --- | --- | --- | --- |
| | Flush adapter | Straight adapter | Angular adapter |
| Number of elements | 4,419 | 3,986 | 10,266 |
| Number of nodes | 1,009 | 980 | 2,367 |
| Maximum frequency (6 elements/wavelength) | 45,374 Hz | 44,593 Hz | 44,199 Hz |

**Table 1.** Meshes data

The FEM models of the three adapters are shown in Figs. 4a, 4b and 4c. The cavity's transfer functions are calculated by imposing prescribed nodal pressures in the nodes marked with small green arrows. In order to save time and computational efforts, a modal solution method is adopted using the first 14 modes. A modal damping of 5% is considered in these calculations.



(a)                    (b)                    (c)
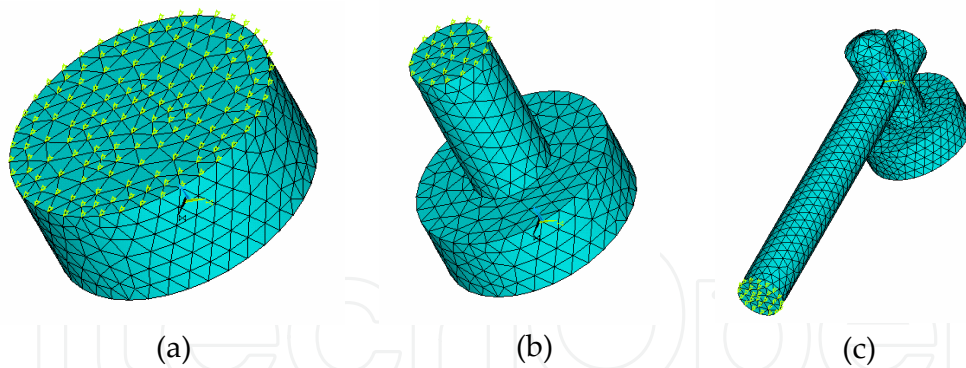
**Figure 4.** a) Flush adapter mesh; b) Straight adapter mesh; c) Angular adapter mesh

## 2.2. Experimental set up

An experimental unit is conceived to characterize all three adapters, as shown in Fig. 5. The experimental unit is placed into an acoustic reverberant chamber and submitted to an ADF, with a frequency profile shown in Fig. 6, which impinges the plate where the adapters and microphones/conditioners are installed. Care is taken to assure that the plate has structural response similar to that found along the launcher skin. Accelerometers are installed on the plate to measure the acoustically induced structural vibration.
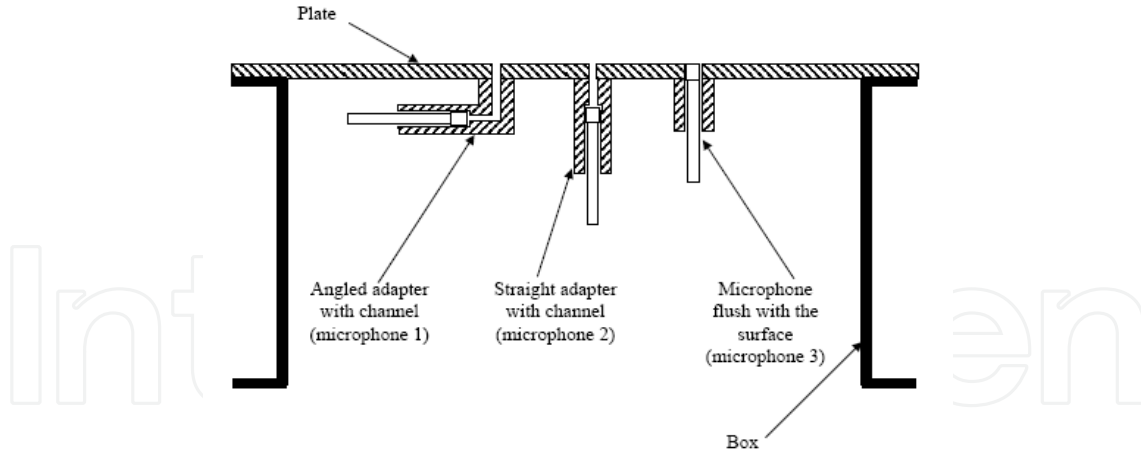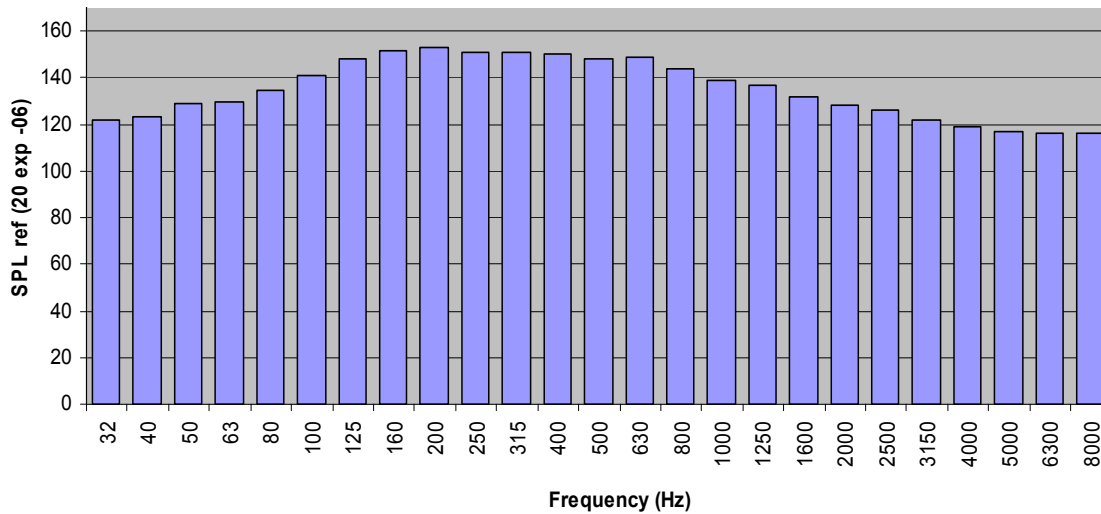
**Figure 5.** Experimental unit



**Figure 6.** Excitation profile Overall Sound Pressure Level (OSPL ) – 160 dB

## 2.3. Methodology for the external measured SPL correction

### 2.3.1. Characterization of the adapters´ cavities

The amplitude-frequency characteristics of such adapters must be accounted to determine the acoustic levels measured during the flight mission, since the device channels operate like filters. The SPL measured by the microphone installed with the flush adapter (Fig. 4a) is considered as the reference. Then the adapters transfer functions relating the input signal given by the microphone with the flush adapter and the output signal given by the microphones with the protective adapters (angular or straight) can be obtained by Eqs. (3) and (4)

$$M1(\omega) = H_{M1}(\omega)M3(\omega) \tag{3}$$

$$M2(\omega) = H_{M2}(\omega)M3(\omega) \tag{4}$$

where: $H_{M1}(\omega)$ and $H_{M2}(\omega)$: angular and straight adapter transfer functions, respectively. $M1$, $M2$, $M3$: measured SPL into angular, straight and flush adapters.

## 2.3.2. Results

Analytical and numerical natural frequencies results are compared with those obtained by acoustic testing in Table 2. As pointed out before, the measured SPL with the flush adapter can be read directly. In this way, only the adapters shown in Figures 4b and 4c are considered.

| | Straight Adapter | | | | Angular Adapter | | | |
|---|---|---|---|---|---|---|---|---|
| Mode | Analytical | FEM | Testing | FEM-Testing Difference (%) | Analytical | FEM | Testing | FEM-Testing Difference (%) |
| 1 | 5,000 | 5,396.6 | 5,202 | 3.74 | 2,300 | 2,204.7 | 1,953 | 12.88 |
| 2 | - | 27,032 | - | - | - | 8,660.3 | 7,831 | 10.58 |

**Table 2.** Theoretical x Experimental natural frequencies (in Hz)

Disagreements between test and predicted resonance frequencies can be explained by possible inaccuracy in microphone installation and complicated shape of the angular channel. The characterization of the adapters´ cavities is performed numerically, by calculating $H_{M1}(\omega)$ and $H_{M2}(\omega)$ (Eqs. (3) and (4)) using FEM. The calculated response functions of the angular and the straight adapter models are compared to those obtained experimentally in Fig. 7 (experimental frequency resolution Δf = 18.78 Hz; numerical frequency resolution Δf = 20.00 Hz).
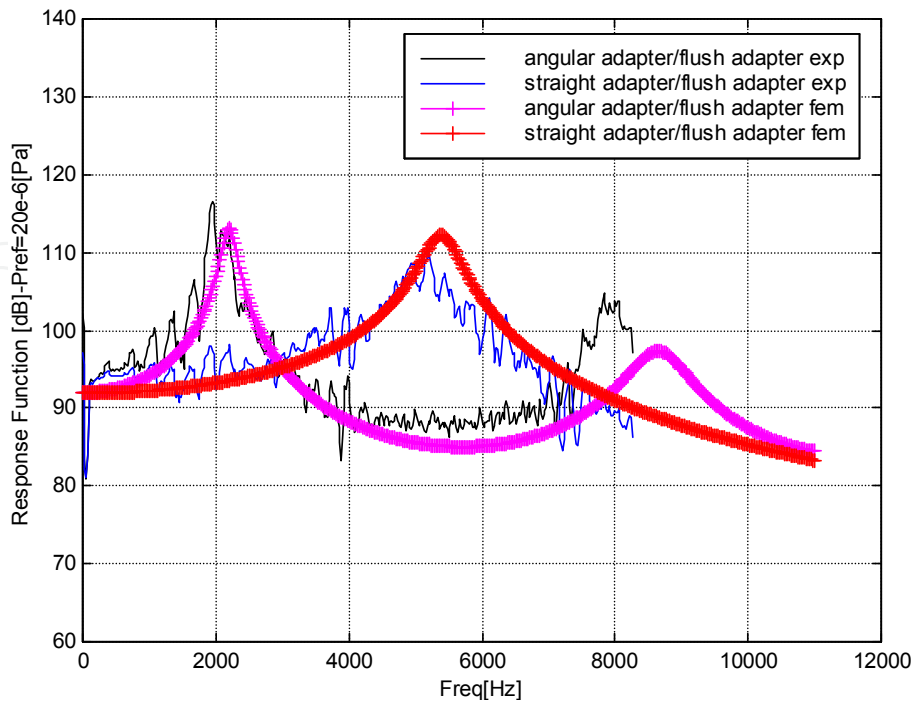


**Figure 7.** Microphones with adapters transfer functions (numerical and experimental)

The theoretical and experimental response functions show good agreement, with a shift in the second resonance peak for the microphone with angular adapter. The errors can be caused by: bad characterization of the ADF spectral distribution into the FEM model; adapter's geometry complexity; microphone installation inaccuracy or a combination of some of these factors.

Equations 3 and 4 show that the external noise (given by $M3(\omega)$) can be identified by knowing the internal noise and the inverses of the transfer functions for the angular and straight adapters.

## 3. Vibro-acoustic modelling of payload fairings (PLF)

A complete survey of PLF vibro-acoustic environment must be carried out, in order to determine its inner SPL. In this respect, it is important to have reliable numerical tools that can predict the responses of ELV systems, subjected to in-flight acoustic loads and that enable NCT design.

Low-frequency coupling techniques are used to estimate a PLF dynamic behavior. The fairing body and its inner acoustic domain are analyzed by using Finite Element Method (FEM) and Boundary Element Method (BEM). Structural FEM/fluid FEM and structural FEM/fluid BEM modeling techniques are then applied. In order to simulate the lift off acoustic excitation, an ADF of 145 dB OSPL is applied on the fairing body and coupled calculations are done from 5 to 150 Hz, which yielded the acoustic and skin responses for both models. Modal expansion and semi-modal expansion model techniques are applied, respectively.

For the high-frequency analysis, it is applied the Statistical Energy Analysis (SEA) technique, for a frequency range from 5 to 8,000 Hz. The 145 dB OSPL excitation is applied to the structural panels of the fairing and the acoustic and structural mean responses are calculated.

In view of validating the numerical predictions for the fairing, acoustic test is done to measure the acoustics inside the PLF. The PLF is submitted to 145 dB OSPL in a 1,200 m³ acoustic reverberant chamber and microphones are positioned in its inner domain.

The implementation of sound absorption blankets is applied as a control technique to attenuate acoustic noise from medium- to high-frequency bands. SEA is a technique for high-frequency analysis; therefore, adequate to assess the influence of blankets on space systems. The generated SEA fluid-structure model is used to calculate internal SPL, with single-, double-, and multi-layered noise control treatments (NCT). Two NCT modeling approaches are used to simulate the effect of blanketing the fairing cavity:

i.   acoustic materials Biot´s parameters, given by the manufacturer;
ii.  material samples absorption coefficient, measured in a Kundt Tube.

### 3.1. Model description

The analyzed fairing is hammerhead type geometry and is composed of the body structure, functional components as electric and pyrotechnic components of the ejection system,

mechanisms as well as the exterior cork liner. Figures 8a and 8b show the Brazilian VLS fairing structure.



|         (a)          |         (b)          |
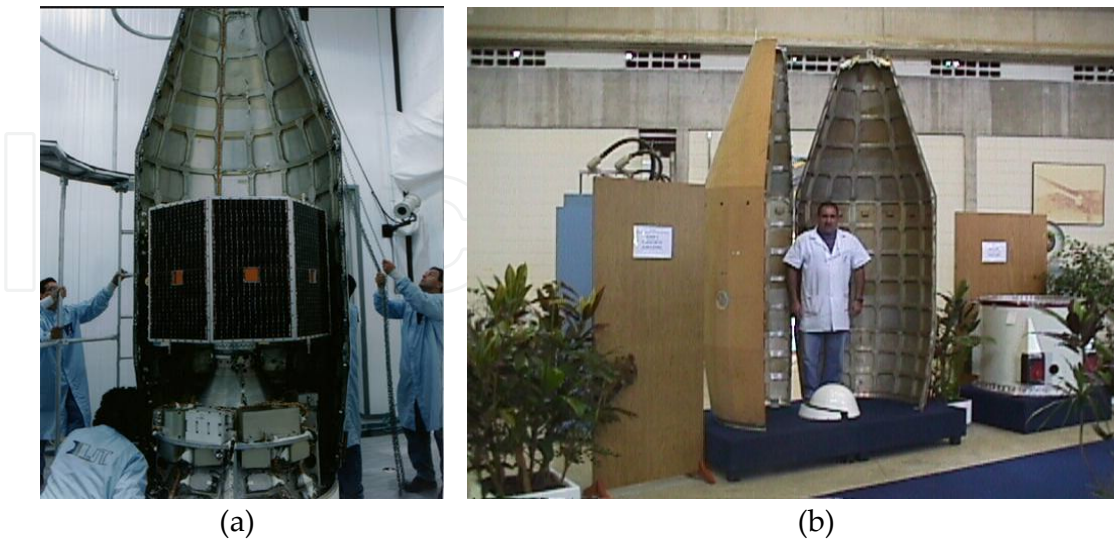
**Figure 8.** a) PLF structure; b) PLF structure

## 3.2. Modelling methodology

### 3.2.1. Low-frequency modeling (deterministic) techniques

In view of predicting the operational fairing cavity SPL, both the dynamic displacements of the fairing structure as well as the acoustic pressure fields at the interior and the exterior side of the fairing should be considered. In this study, however, the fluid-structure coupling interaction between the structural displacements and the exterior acoustic pressure field is neglected. The exterior acoustic pressure is assumed to be a known external excitation for the vibro-acoustic system, consisting of the fairing body and the internal acoustic cavity. The FEM and BEM are the most appropriate numerical techniques for the (low-frequency) dynamic analysis of this type of vibro-acoustic system.

FEM based models for coupled vibro-acoustic problems are most commonly described in an Eulerian formulation, in which the fluid is described by a single scalar function, usually the acoustic pressure, while the structural components are described by a displacement vector. The resulting combined FEM/FEM model in the unknown structural displacements and acoustic pressures at the nodes of, respectively, the structural and the acoustic FEM meshes are [20],

$$\left( \begin{bmatrix} K_S & K_C \\ 0 & K_A \end{bmatrix} + j\omega \begin{bmatrix} C_S & 0 \\ 0 & C_A \end{bmatrix} - \omega^2 \begin{bmatrix} M_S & 0 \\ -\rho K_C^T & M_A \end{bmatrix} \right) \begin{Bmatrix} w_i \\ p_i \end{Bmatrix} = \begin{Bmatrix} F_{Si} \\ F_{Ai} \end{Bmatrix} \tag{5}$$

Where:

$K_S$ – Structural stiffness matrix $M_S$ – Structural mass matrix $C_S$ – Structural damping matrix $K_C$ – Fluid – structure coupling matrix

$M_A$ – Fluid mass matrix $K_A$ – Fluid stiffness matrix $C_A$ – Fluid damping matrix
$w_i$ – Structural displacements nodal vector $p_i$ – Acoustic pressures nodal vector
$F_{Si}$ – Force nodal vector $F_{Ai}$ – Acoustic sources nodal vector

In comparison with a purely structural or purely acoustic FEM model, the coupled stiffness and mass matrices (Eq. (5)) are no longer symmetrical due to the fact that the force loading of the fluid on the structure is proportional to the pressure, resulting in a cross-coupling term $K_C$ in the coupled stiffness matrix, while the force loading of the structure on the fluid is proportional to the acceleration, resulting in a cross-coupling term $M_C = -\rho K_C^T$ in the coupled mass matrix.

Low-frequency vibro-acoustic problems can also be modeled by describing the structural behavior in a FEM model and the fluid behavior in a BEM model. In the same way as in the FEM/FEM technique, deterministic FEM/BEM models are usually described by acoustic double layer potential and structural displacement, which are the field variables. Equation (6) presents the resulting combined FEM structural displacements and BEM acoustic pressure differences at the nodes, for a coupled FEM/BEM mesh [23].

$$\begin{pmatrix} K_S + j\omega C_S - \omega^2 M_S & L_C \\ L_C & \dfrac{D}{\rho_0 \omega^2} \end{pmatrix} \begin{Bmatrix} w_i \\ \mu_i \end{Bmatrix} = \begin{Bmatrix} F_{Si} \\ F_{Ai} \end{Bmatrix} \qquad (6)$$

Where $L_C$ is the fluid-structure coupling matrix, $D$ is the BEM acoustic matrix of coefficients and $\mu_i$ is the nodal vector of double layer potentials.

In deterministic models, the dynamic variables within each element are expressed in terms of nodal shape functions, usually based on low-order (polynomial) functions. Since these low-order shape functions can only represent a restricted spatial variation, a large number of elements is needed to accurately represent the oscillatory wave nature of the dynamic response. A general rule of thumb states that for fluid-structure interactions, at least 6 (linear) elements per wavelength are required to get reasonable accuracy. Since wavelengths decrease for increasing frequency, the FEM model sizes, computational efforts and memory requirements increase also with frequency. As a result, the use of FEM and BEM models is practically restricted to low-frequency applications. In comparison with uncoupled structural or acoustic problems, this practical frequency threshold becomes significantly smaller for coupled vibro-acoustic problems, since a structural and an acoustic problem must be solved simultaneously. Moreover, the matrices in a coupled model are no longer symmetrical, so that less efficient non-symmetrical solvers must be used. As a consequence, the computational effort, involved with the use of coupled FEM/FEM and FEM/BEM models for real-life vibro-acoustic engineering problems, becomes large at very low frequencies.

In order to obtain coupled vibro-acoustic response predictions within reasonable computational efforts, the dimensions of the FEM/FEM problem (Eq. (5)) have to be reduced. The most applied technique for model reduction is the modal superposition technique, which expresses the unknowns of the system in terms of a modal basis, resulting

in a set of unknown modal participation factors, whose size is much smaller than the size of the original set of unknowns. A modal expansion in terms of uncoupled structural and acoustic modes is performed by using computationally efficient symmetric eigenvalue algorithms and requires much less computational effort than the use of vibro-acoustic (coupled) modes. However, a large number of high-order uncoupled acoustic modes is required to accurately represent the normal displacement continuity along the fluid-structure interface.

In a FEM/FEM virtual prototype, a modal expansion in terms of uncoupled structural and uncoupled acoustic modal bases is used, in order to keep the computational efforts within reasonable limits. On one hand, structural wavelengths are much smaller than acoustic wavelengths, so that the structural FEM mesh of the fairing must be finer than the acoustic FEM mesh of the inner cavity. On the other hand, due to the continuity of the normal structural and fluid displacements along the fluid-structure coupling interface, both meshes must be compatible in this region. In this framework, the following modeling methodology is adopted: 1) A fine FEM mesh of the fairing is used for the construction of the uncoupled structural modal data basis. 2) The resulting modes are then projected onto a FEM coarse mesh of the fairing structure. 3) For the acoustic cavity FEM mesh, the same mesh density is used along the fluid-structure coupling interface as the PLF structural coarse mesh, while the mesh density is slightly decreased towards the central axis of the cavity. 4) The uncoupled modes, resulting from this acoustic FEM mesh, together with the projected structural modal basis are used in a coupled FEM/FEM model. It is important to highlight that the coarse structural mesh has only the shells of the fairing structure, while all reinforcing beams are omitted, since it is assumed that these stiffeners have no significant effect on the fluid-structure coupling interaction, while their presence would increase the computational load of the modeling process.

For the case of the FEM/BEM problem (Eq. (6)), the modal expansion cannot be used, since the frequency dependency of the matrix coefficients in the acoustic part prohibits a standard eigenvalue calculation. Such as, the semi-modal approach, which uses only the expansion of the structural modal data basis, is applied. As mentioned above, BEM drawbacks as fully population of the matrices, complex and frequency dependent models result in a coupled FEM/BEM model less efficient than coupled FEM/FEM model. Therefore, the rule of thumb of 6 (linear) elements per wavelength becomes prohibitive for the actual fairing fluid-structure study. Such a way, a coarsest structural mesh may be generated and the same adopted frequency range for FEM/FEM model is kept for this FEM/BEM model, even considering that the structure has not enough discrete density. However, the modal data basis calculated using the structural fine mesh can assure good results for the structural displacements, in this fluid-structure model, since the expansion in terms of such a data basis is used on these Frequency Response Analysis (FRA) computations. The displacement continuity of the structural and acoustic meshes (same density in the fluid-structure interface) is considered to perform the link and calculate the coupled dynamic skin displacements and acoustic cavity pressure responses, for both FEM/FEM and FEM/BEM models.

### 3.2.2. High-frequency modeling (statistical) technique

A characteristic of high-frequency analysis is the uncertainty in modal parameters. The resonances and mode shapes show great sensitivity to small variations of geometry, construction and material properties. In addition, programs used to evaluate mode shapes and frequencies are known to be inaccurate for higher modes. In light of these uncertainties, a statistical model of the dynamic parameters seems natural and appropriate. As an alternative method for higher frequency analysis of the inner cavity of fairings, Statistical Energy Analysis (SEA) approach is proposed. This approach is the description of the dynamic system as a member of a statistical population or ensemble, whether or not the temporal behavior is random. SEA emphasizes the aspects of this field dynamical study.

The SEA equations express the energy balance of different subsystems in a model [24]. Some subsystems have direct power input of an independent source, e. g. an excitation force on a structural component, a sound power source in an acoustic medium etc. In general, subsystems can receive power (input power from external sources), dissipate power (internal losses due to damping) and exchange power with other subsystems to which they are coupled (losses due to coupling). SEA fundamental hypothesis as dissipation losses in relation to the energy variable and modal energy proportionality from connected subsystems are used to yield the SEA matrix equation of complex structures. The distribution of the dynamical response in the system due to some excitation is obtained from the distribution of the energy among the mode groups, based on a set of power balance equations for the mode groups.

## 3.3. FEM structural meshes

The fairing body is divided in five surfaces. The surfaces are discretized by using 4-noded quadrilateral shell elements, while 2-noded beam elements are used for the circumferential and the axial stiffeners. To account for the mass of the cork blanket on the exterior fairing surface, a distribution of concentrated mass elements are attached to the fairing nodes.

A total of 174 structural modes in a frequency range up to 220 Hz have been identified. Table 3 describes the main structural modes calculated by using FEM in the range up to 150 Hz.

| mode | frequency (Hz) |
|---|---|
| first bending | 38.637 |
| first breathing | 77.821 |
| second breathing | 92.694 |
| first longitudinal | 108.749 |
| first torsion | 125.772 |
| second bending | 150.735 |

**Table 3.** Fairing body structural modes

Table 3 shows that the first structural bending mode of the fairing is identified at 38.6 Hz, while the second mode is at 150.7 Hz. Figures 9a and 9b show the referred structural modes.



(a)                                                              (b)
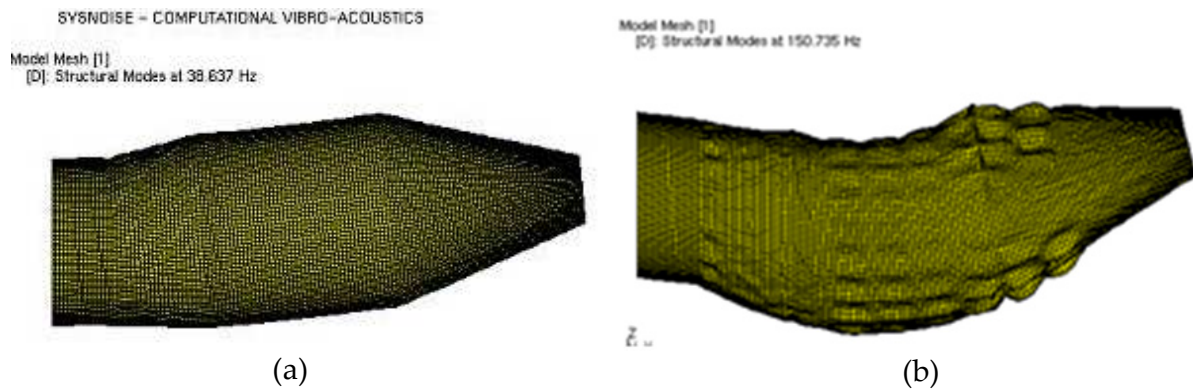
**Figure 9.** a) First structural bending mode; b) Second structural bending mode

## 3.4. FEM and BEM acoustic meshes

The acoustic FEM mesh consists of 119,577 nodes and 110,238 elements (106,050 8-noded hexahedral elements and 4,188 6-noded pentahedral elements). The cavity is considered filled with air at 15° C. The cavity's bottom and top faces are assumed to be acoustically closed (rigid walls). The acoustic mesh generation takes into account the meshes compatibility on the fluid-structure interface.

A total of 80 acoustic modes in a frequency range up to 566 Hz were identified. Acoustic wavelengths are bigger than structural wavelengths. Such that, a large number of high-order uncoupled acoustic modes is required to accurately represent the normal displacement continuity along the fluid-structure interface. That is why higher frequency range is used to describe the acoustic modal behavior of the fairing. Table 4 describes the acoustic modes in the frequency range up to 150 Hz.

| Mode | Frequency (Hz) |
|---|---|
| rigid body | 0.000 |
| first longitudinal | 63.491 |
| second longitudinal | 112.129 |

**Table 4.** Fairing cavity acoustic modes

It can be noticed in table 4 that the first and second acoustic modes of the fairing cavity are identified at 63.5 Hz and 112.1 Hz, respectively. Figures 10a and 10b show the referred acoustic modes.

The BEM acoustic mesh is a 2-D coarsest mesh. Therefore, as the coupled FEM/BEM equation is frequency dependent (Eq. (6)), the acoustic modes are not considered in the acoustic pressure calculations (semi-modal reduction model).
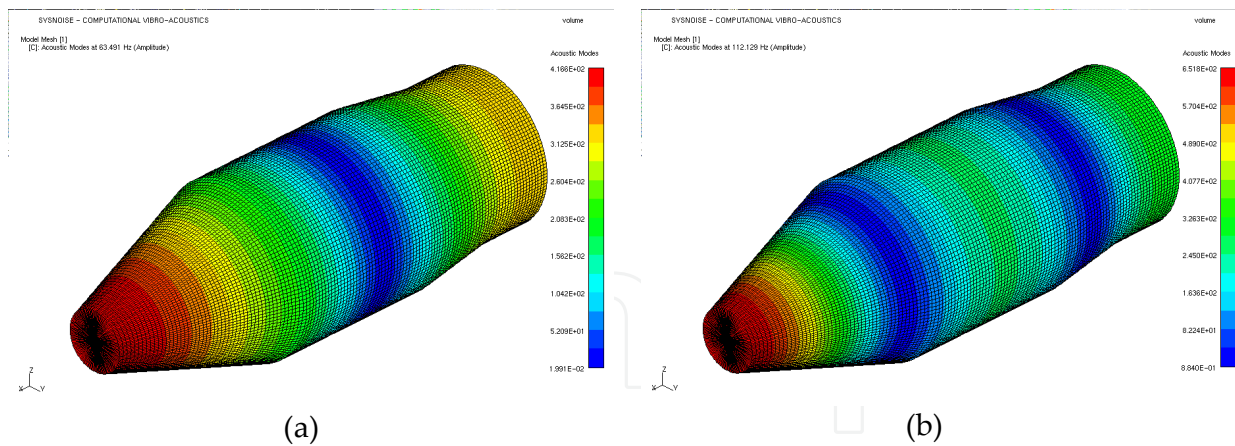
**Figure 10.** a) First acoustic longitudinal mode; b) Second acoustic longitudinal mode

## 3.5. Model excitation

A uniform pressure loading is simulated by applying a normal point force varying harmonically on all nodes of the fairing shell elements. The force value is defined such that the total load is equivalent to a uniform pressure of 145 dB OSPL. Link of the acoustic and structural parts is done as well as the structural modal data basis is projected to the coarse and coarsest meshes.

In this way, all the meshes, modal data bases and excitation, needed to perform low-frequency calculations, using coupling fluid-structure techniques are ready. Next step is to perform FRA calculations for both models.

## 3.6. SEA fairing vibro-acoustic model

The fairing body is divided in four surfaces, as shown in Fig. 11a. To account for the rib-stiffened plates of the surfaces 2, 3 and 4, the SEA structural fairing model considers connected plates and beams (longitudinal and circular). The plate structural subsystems are generated as singly curved shells and uniform plates. Shell surface 1 has a thickness of 3mm and is modeled as a simple plate of aluminum (E=72 GPa, ν=0.29, ϱ=2750 kg/m³), while the other three surfaces are 0.8 mm thick and made of an aluminum alloy (E=72 GPa, ν=0.29, ϱ=7000 kg/m³). The circular and longitudinal beams are modeled by assigning the same material as the shells of the surfaces 2, 3 and 4 (Figure 11a). Damping loss factors of 1% (for flexure, extension and shear propagating waves) are assigned to the plates and beams subsystems, in order to account for the internal loss factors.

A total of 72 beams (44 longitudinal and 28 circular) and 8 shells (02 singly curved shells of the adaptor, 02 singly curved shells of the lower cone, 02 singly curved shells of the main cylinder and 02 singly curved shells of the upper cone) compose the structural SEA model. Figure 11a shows the SEA plates and beams generated to model the VLS-1 fairing structure. The external blanketed treatment of cork on the surfaces 2, 3 and 4, was simulated in this model as material addition. The layered area and the density of the cork were considered to assign this mass.

The acoustic environment inside the fairing was generated by starting from the structural model. This acoustic cavity was created considering air at 15° C as the fluid as well as the dimensional parameters of the fairing. The top and bottom face of the cavity were assumed to be acoustically closed. Figure 11b presents the 3D acoustic cavity of the fairing.



(a)                                                            (b)
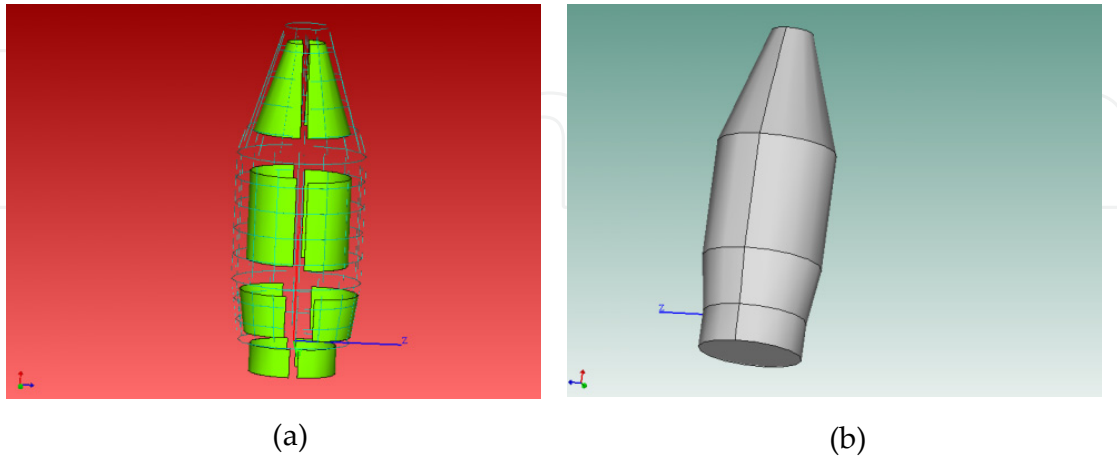
**Figure 11.** a) Structural subsystems (shells, circular beams and longitudinal beams) b) Acoustic cavity of the fairing

The coupling boundary between all the structural and acoustic subsystems is modeled to consider the transmission of power across the junctions. A junction is comprised of connections to any number of coincident subsystems. As a result, all the subsystems that share common nodes are connected by point, line and area junctions and all the appropriate wavefields are connected as well as the corresponding coupling loss factors (CLF) between subsystems are created.

The estimated sound pressure levels at the lift off are assigned to the SEA model. Only elements with large surface areas, as plates and panels, are considered to be susceptible to acoustic excitation ([11], [24] and [25]). An ADF of 145 dB OSPL (Fig. 12) is applied to the plates of the SEA fairing model, which simulates the power input into a structural plate or shell element.

## 3.7. Analysis results

In view of having a complete knowledge of the fairing dynamic vibro-acoustic behavior, the fairing structural skin as well as its inner acoustic domain responses should be presented. However, since this chapter concerns acoustics, the body structural displacements are not presented here. Below, the obtained results of the acoustic behavior applying vibro-acoustic low-frequency and high-frequency analysis techniques predictions are presented.

### 3.7.1. Low-frequency techniques

#### 3.7.1.1. FEM/FEM response calculations

A modal expansion in terms of 174 uncoupled structural and 80 uncoupled acoustic modes is used for the coupled calculations. A modal damping of 1% is assigned to all structural

modes. All calculations are performed with a frequency resolution of 1 Hz. Figure 13 shows the low-frequency acoustic pressure spectra of the PLF for the case of a uniform exterior pressure loading, using FEM/FEM coupling analysis. It can be seen that the low-frequency pressure is dominated by the first longitudinal mode around 63.5 Hz and the second longitudinal mode around 112.1 Hz.

### 3.7.1.2. FEM/BEM response calculations

The same structural modal expansion as used for FEM/FEM is used for this FEM/BEM response calculations. Due to the frequency dependency of the boundary integral equation, the acoustic modal basis can not be used. A damping of 1% is assigned to all structural modes. All calculations are performed with a frequency resolution of 2 Hz. Figure 13 presents a comparison of the computed inner cavity space averaged acoustic pressure using FEM/FEM and FEM/BEM techniques.

### 3.7.2. High-frequency technique

The energy balance (levels and interactions) between different subsystems of the SEA model is calculated. The interest frequency range is 5 to 8,000 Hz, by third octave bandwidth. As mentioned before, SEA technique is more effective in higher frequencies, where dynamic systems present higher modal density. The vibro-acoustic responses of the fairing, using SEA technique, are shown in Fig 13.

It is important to highlight that for the low-frequency range, SEA analysis results are not reliable, since the accuracy of the SEA technique is proportional to the modal density [24].
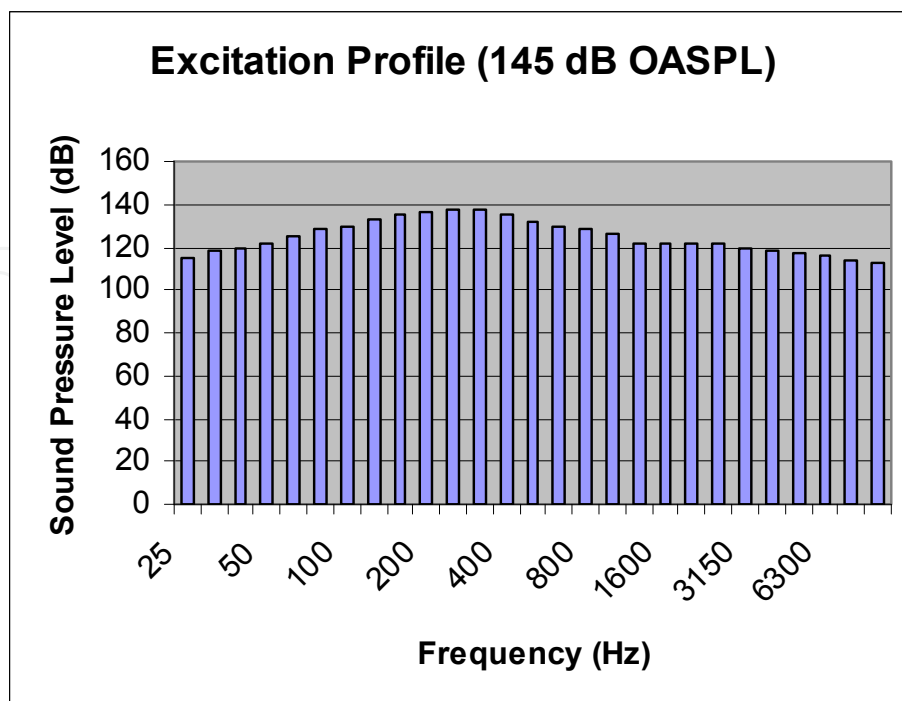


**Figure 12.** Acoustic diffuse field at lift off
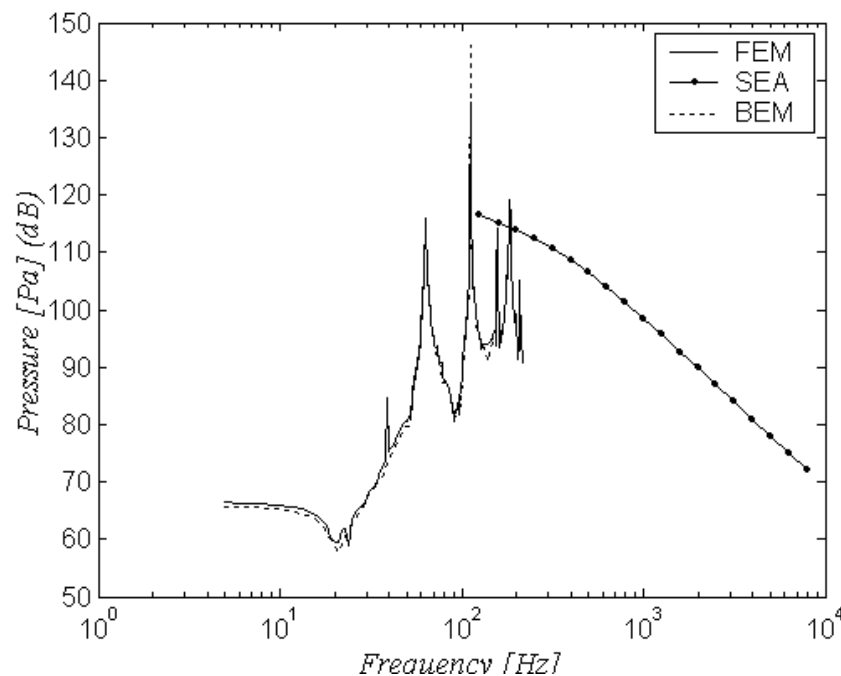
**Figure 13.** Acoustic Response Inside PLF

Considering the accuracy, advantages and drawbacks of the deterministic and statistical techniques, each of them is successfully applied in different frequency ranges. Such that, for the analyzed PLF, valid response results using deterministic techniques are assumed up to 150 Hz, while valid SEA results are assumed from 300 up 8,000 Hz. It is important to mention that in the "twilight zone" or medium frequency bandwidth (from 150 to 300 Hz), where deterministic models are inaccurate and present prohibitive computation time for the calculations and where the high modal density requirement is not yet accomplished for SEA, both results may be considered, as shows figure 13.

### 3.8. Model validation

The fairing structure was positioned inside an acoustic chamber and excited with an ADF of 145 dB OSPL. Eight control microphones were positioned inside the reverberant chamber, which feedback the control system. Four measurement microphones were located in the acoustic cavity of the PLF. The measured space averaged SPL is compared with the theoretical acoustic responses, computed using the virtual prototypes (FEM and SEA models) (Fig. 14).

The calculated internal acoustic frequency response function shown in figure 13 may be transformed into 1/3 octave band responses to be compared with the experimental (measured) results. Figure 14 presents the 1/3 octave comparisons for the frequency bandwidths ranging from 31.5 up to 8,000 Hz. It can be noticed, that experimental and calculated low-frequency responses have good agreement, presenting more significant differences only on the 1/3 octave bands 31.5, 40 and 50 Hz. This is because the low-

frequency modes of the acoustic chamber are not well excited. However, in the regions where the cavity response is dominant (63 Hz and 112 Hz), differences are pretty small.
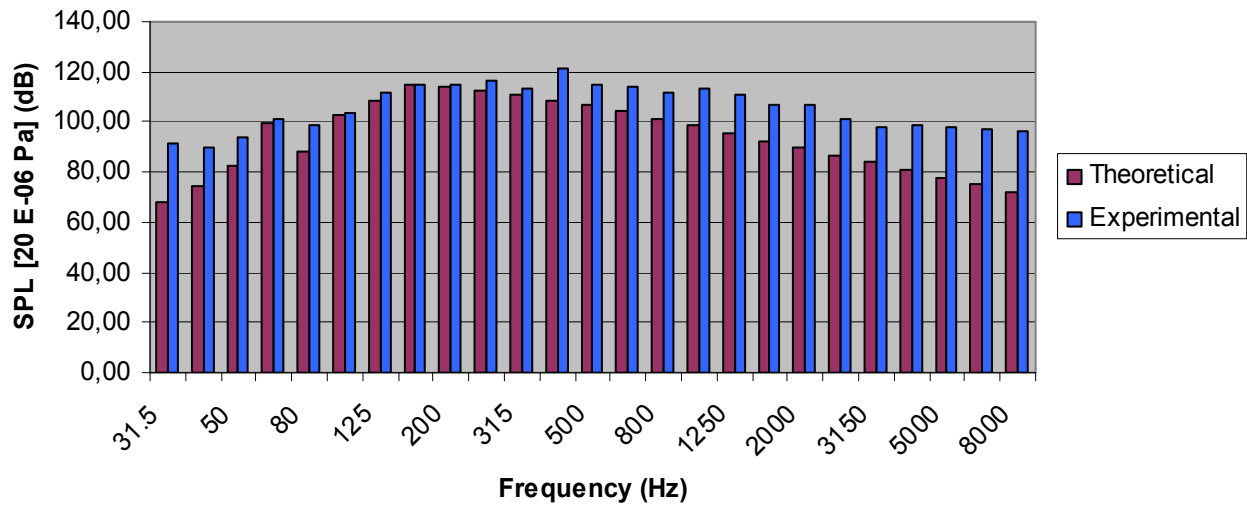


**Figure 14.** High-frequency theoretical X experimental comparison

For the higher frequencies, a more reasonable comparison should be done using Power Spectral Density (PSD) [28], since SEA calculations may be interpreted as mean values of energetic response functions when averaged at a given frequency over an ensemble of similar systems, differently of peak values resulting from deterministic approaches. However, a qualitative comparison can be presented for 1/3 octave bands from 160 up to 8,000 Hz, since one keeps in mind that mean values and the predicted magnitudes yielded by SEA should under estimate the dynamic response with a certain (acceptable) variance. Valid SEA results are assumed from 300 up 8,000 Hz, since the minimum five modes by bandwidth (modal density) requirement becomes true starting from 300 Hz.

At the beginning phases of space projects, the assessment of the effect of using different passive techniques for acoustic environment alleviation to be applied to PLF is an important issue. One of the main applications of numerical control prediction is the decision, still in the early product development phase, which design version is the most appropriate from the noise control point of view. By introducing the concept of sensitivity analysis, product development can be performed in a more systematic way. In order to predict the efficiency of a NCT, one compares the effects of design modifications.

In this framework, different blanket layers are implemented on the PLF elasto-acoustic virtual prototype and the effects of these NCT implementations are assessed. Since blankets acoustic absorption depend on certain material parameters, two blanket modeling approaches are assessed as follows: material physical Biot´s parameters as density, porosity, resistivity, tortuosity, viscous and thermal characteristic lengths, given by the blanket manufacturer and measured normal incidence absorption coefficients of material samples.

Furthermore, the influence of the NCT thicknesses and the presence of air-gaps between blankets are analyzed. Biot's parameters and absorption coefficient approaches are implemented in the coupled elasto-acoustic SEA model of the PLF.

For the Biot's parameters approach, an explicit model of the inserted material is considered, based on the physical properties of individual layers, which are accounted in the SEA model. Six types of glass wools are analyzed and the SPL inside the fairing are calculated. The wools' densities are given in pounds per cubic feet (pcf - 1 lb/ft$^3$ = 16.02 Kg/m$^3$). A thickness of 7,62 cm is adopted for almost all glass wools, but the two 1.2pcf glass wools, that presents particular behavior, which adopted thicknesses were 0.19 cm and 0.38 cm. The best performing material is chosen and a comparison between different thicknesses and percentages of layered surfaces of the fairing is done, considering the final weight of the applied NCT. The materials used were glass wools described in Table 5. The wools' Biot's parameters can be found in [4].

| Material characteristcs | | | | | | |
|---|---|---|---|---|---|---|
| Density (pcf) | 0.34 | 0.42 | 0.60 | 1.20 | 1.20 | 1.50 |
| Thickness (inches) | 3.00 | 3.00 | 3.00 | 0.75 | 1.50 | 3.00 |

**Table 5.** Glass wools used

On the other side, the measured absorption coefficient of multi- and single-layered samples of glass wools of 0.42 and 1.0 pcf were considered. According to [26], air gaps between materials increase the acoustic absorption at low-frequencies. For this case, samples with two different air gaps are positioned into a Kundt tube. The single-layered samples are 3.50 cm thick, while combinations are done with samples of 1.75 cm thick. Other configurations were assembled with air gaps of 1.0 and 3.0 cm between samples. Figure 15 shows the sample combinations. All the measured absorption coefficients are shown in Fig. 16. These absorption coefficients are assigned on the fairing vibro-acoustic model and SPL are calculated.

The PLF acoustic responses for different NCT configurations are shown in Fig. 17. Notice that the insertion of the 0.34pcf glass wool – 7.62 cm yields almost 20 dB of attenuation (chosen as the best performing material). The assessment of the thickness influence is done by assigning 0.34pcf glass wools of 7.62, 10.16 and 12.7 cm thicknesses, with total NCT weights of 3.90, 5.30 and 6.60 Kg, respectively. Figure 18 shows the internal SPL one-third octave distribution, as well as the OSPL.

Figure 19 shows SPL and OSPL from 50 to 8,000 Hz, for the NCT described in Fig. 16, without air gaps. A 3.50 cm double-layered blanket (0.42pcf/1.0pcf) is compared with two single-layered NCT. Notice in this figure that NCT decrease the internal OSPL from 132 dB to 128 dB. Figure 20 shows that single-layered treatment with 1.0 pcf and air gaps presented better results. One can see the air gap effect, since the SPL close to 100, 315 and

500 Hz are higher mainly when the 1.0 pcf material with 3.0 cm air gap is applied. The calculations yielded 127.5 dB OSPL inside the fairing cavity. This means that a gain of approximately 3.0 dB at 100 Hz bandwidth can be obtained, yielding an overall gain of 1.0 dB, approximately. However, air gap installation can be limited, due to fairing internal space. In this case, it is preferable to install the blanketed treatment distant from the panels by small air gaps, instead of bonded, once this installation configuration presents higher transmission loss [10].



**Figure 15.** Double-layered 0.42pcf (yellow)/1.0pcf (orange), 1.75 cm thick each.
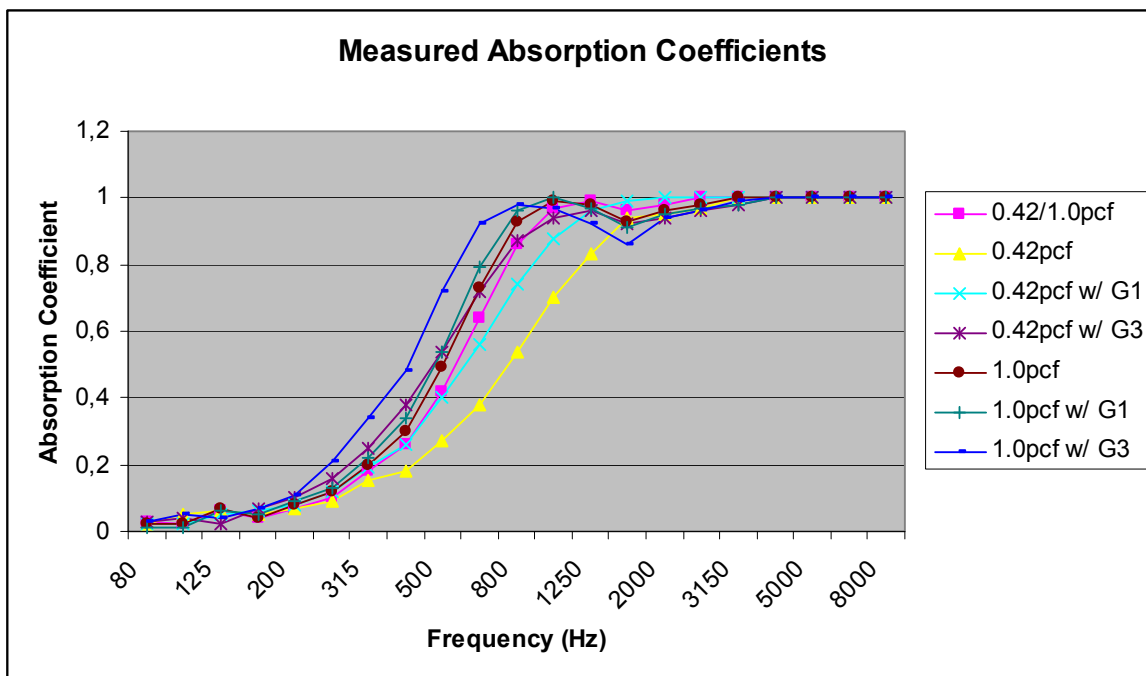


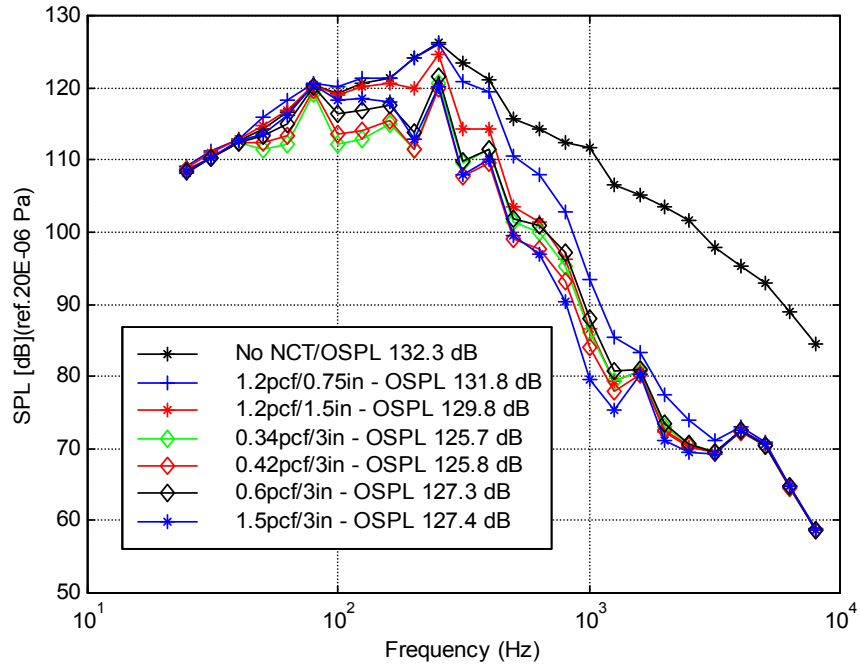**Figure 16.** Measured absorption coefficients*G1 and G3: air gaps of 1.0 cm and 3.0 cm
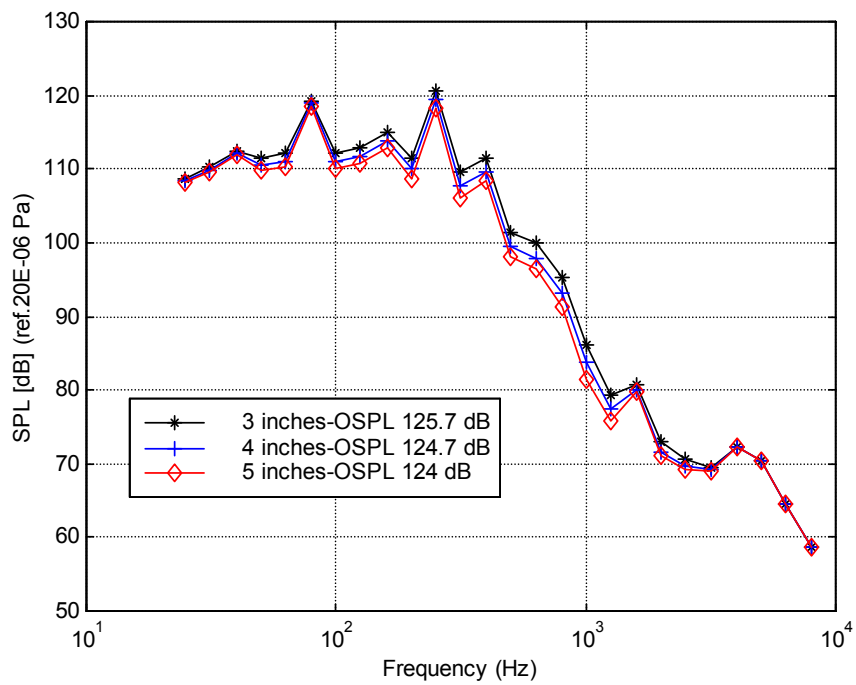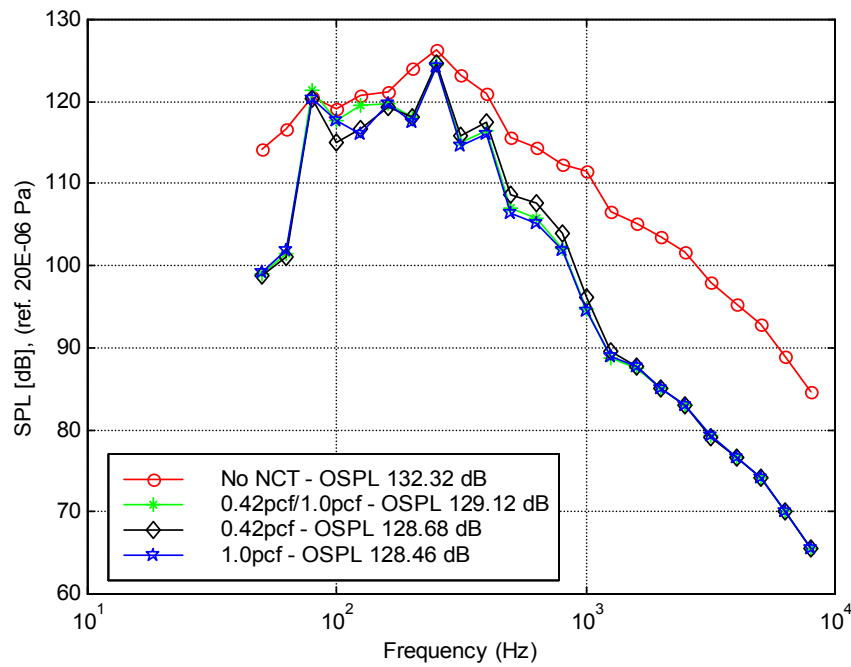
**Figure 17.** SPL for different blankets
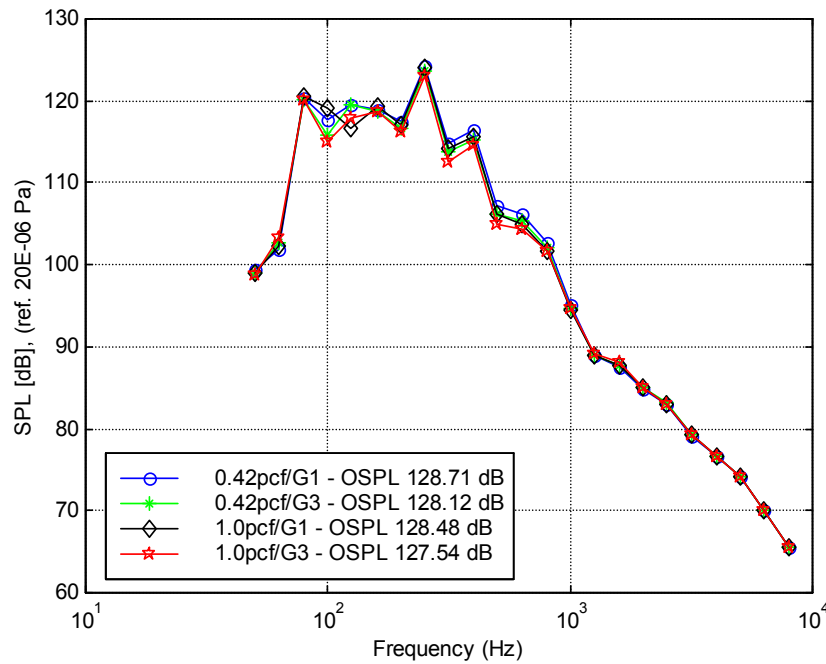


**Figure 18.** SPL for different thicknesses

**Figure 19.** SPL for NCT without air gap.



**Figure 20.** SPL for NCT with air gaps (*G1 and G3: air gaps of 1.0 cm and 3.0 cm)

## 4. Combustion instabilities of liquid propelled rocket engines due to chamber combustion acoustics

Combustion instabilities have been present in the development of LPRE over the last decades. There are basically three types of combustion instabilities: low-frequency (LF), medium-frequency (MF) and high-frequency (HF). LF instabilities, also called chugging, are

caused by pressure interactions between the propellant feed system and the combustion chamber. MF instabilities, also called buzzing, are due to coupling between the combustion process and the propellant feed system flow. The HF instabilities are the most potentially dangerous and not well-understood ones. It occurs due to coupling of the combustion process and the chamber acoustics [27].

The presence of acoustic combustion instabilities must be considered still in development phase, although combustion instabilities can be clearly identified only during firing tests. In [13], it was described that instability can be verified when the power spectrum of the acoustic pressure levels, measured during burning tests, is analyzed. When an oscillation is observed, i.e., combustion instability, sound pressure peaks with well-defined magnitudes summed to the background noise are present. These peaks are correlated to the resonance frequencies of the combustion chamber. This phenomenon can cause instabilities and consequent unexpected behavior such as efficiency loss or even explosion of the engine. In this framework, the engine acoustic cavity characterization becomes an important issue to be investigated.

Acoustic behaviour of chambers is usually determined by doing cold tests measurements (without combustion). Acoustic dynamics in combustion environments are obtained by shifting the cold test resonant frequencies by a scalar factor defined by the ratio of sound velocity at the cold test temperature and at real operation temperature [15].

In view of attenuating acoustic pressure oscillations inside combustion chambers, reactive techniques as Helmholtz Resonators (HR), among others, are widely used ([13] and [16]). These devices are specially designed to attenuate oscillations at discrete resonance frequencies (pure tones). HR have been applied as combustion stabilization devices for solid motors and liquid rocket engines, with success. It could be noted in literature that they are used in a set of dozens or even hundreds in each chamber cavity, distributed along the walls or in a single row along the injector periphery [28].

This item describes a procedure for cold test acoustic characterization of LPRE combustion chambers. Firstly, the acoustical dynamic characterization of a combustion chamber is done and a typical longitudinal resonant frequency is chosen to be attenuated. A HR is designed (tuned at the chosen frequency) and applied to the mock up face plate. A LPRE mock-up [14] was used as experimental model. This test rig faithfully represents the internal acoustic cavity of the original engine. This procedure is followed by doing virtual prototypes of the combustion chamber. The acoustic natural frequencies and mode shapes are numerically calculated by a FEM model and validated through acoustic experimental modal analysis [29].

## 4.1. Experimental Acoustic Modal Analysis (EAMA)

Experimental Modal Analysis (EMA) is a well-applied technique in structure dynamics. However, due to the development of commercial acoustic sources, EAMA can be a suitable choice in view of extracting the acoustical Frequency Response Functions (FRF). In addition,

the mathematical approach of structures modal parameters extraction can be applied to acoustic systems. [29].

In order to check the mutual orthogonality among modes from a modal model and to compare modes between different modal models (i.e., experimental and numerical solutions), the Modal Assurance Criterion (MAC) was used. This criterion indicates the degree of linear dependence between two eigenvectors and can be described as Eq. (7) [30].

$$MAC_{ijm} = 100 \cdot \frac{\left| \{\phi_{im}\}^T \{\phi_{jm}^*\} \right|^2}{\{\phi_{irm}\}^T \{\phi_{im}^*\} \{\phi_{jm}\}^T \{\phi_{jm}^*\}} \tag{7}$$

where: indexes $i$ and $j$ denotes modes obtained by different methods.

## 4.2. Helmholtz resonator

Helmholtz Resonators are widely applied in order to suppress or attenuate the acoustic pressure inside cavities, rooms and other volumes. A HR consists of a small volume connected to a bigger cavity (the combustion chamber, in this case) through an orifice by a flanged neck. The dimensions of the HR must be much smaller than the acoustic wavelength of interest, in order to consider the resonator as lumped elements coupled to a geometric discontinuity. The coupling condition is that the oscillatory volume flow in the neck is equal to that imposed on the fluid inside the cavity, neglecting the elastic property of the air in the neck [30].

A typical HR is shown in Fig.21 (left), being $d$ the neck diameter, $D$ the cavity diameter, $V_c$ the volume cavity, $l$ the neck length and $L$ the cavity length. $P_1$ is the incident acoustic pressure and $P_2$ is the cavity pressure. The gas motion in the HR coupled in an acoustic cavity can behave equivalently to a mass-spring-dashpot system (Fig.21, centre). The system can be divided into three distinct elements. The fluid enclosed in the neck behaves as an uncompressible gas, and its mass correspond to the $m$ element of the mechanical system. The air inside the cavity is compressible and stores potential energy, representing the mechanical stiffness $k$. The mechanical damping element ($c$) is represented by two factors: (i) the open-end of the neck radiates sound, introducing a radiation resistance and (ii) the gas movement in the neck introduces a viscous resistance. Considering the electrical analogue (Fig.21 right), the acoustic compliance $C$ (analogous to electrical capacitance) is related to the stiffness of the air in the cavity, the acoustic inertance $M$ (analogous to electrical inductance) is associated to the inertia element (mass) and the acoustic resistance $R$ (analogous to electrical resistance) is related to the dissipative components stated above.

Considering that the gas beyond the end of the neck moves as a whole with the gas inside the neck, it is necessary to use an effective length $l_{eff}$ which is bigger than the true length $l$ of the neck [19]. The effective length $l_{eff}$ is obtained by adding a mass end correction δ, which is

empirically determined. In [28], it was presented a complete set of recommended equations for mass end correction, depending on the adopted considerations. For the purpose of this work, the appropriated equation is defined by:

$$\delta = 0.85d\left(1 - 0.7\sqrt{AR}\right) \text{for } AR < 0.16 \tag{8}$$

where $AR$ is the Area Ratio ($A_n / A_c$), being $A_n$ and $A_c$ the neck cross-sectional area and the cavity cross-sectional area, respectively. The effective length is calculated as $l_{eff} = l + \delta$.
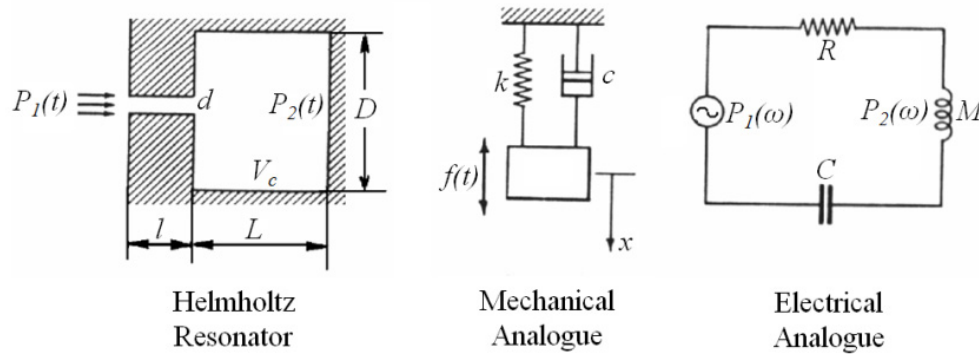


**Figure 21.** Helmholtz Resonators scheme and its analogues

The definition of acoustic inertance ($M$) applied to the Helmholtz resonator gives:

$$M = \frac{m}{A_n^2} = \frac{\rho l_{eff} A_n}{A_n^2} = \frac{\rho l_{eff}}{A_n} \tag{9}$$

where $\rho$ is the air density and $m$ is the effective mass.

The acoustic compliance $C$ is defined as the volume displacement that is produced by the application of unit pressure [19]. By applying this definition to HR, one obtains:

$$C = \frac{V_c}{\rho c^2} \tag{10}$$

where $c$ is the velocity of sound.

The acoustic resistance in the neck ($R$) was approximated as the dissipation associated with viscous forces, considering the dynamic viscosity $\mu$ [28]:

$$R = \frac{8\pi\mu l}{A_n} \tag{11}$$

The acoustic impedance $Z$ of the HR is:

$$Z = R + j\left(\omega M - \frac{1}{\omega C}\right) \tag{12}$$

As can be seen, the acoustic impedance is determined by the geometric and mechanical properties of the resonator. The resonance will occur when the acoustic reactance equals zero:

$$\omega M - \frac{1}{\omega C} = 0 \tag{13}$$

The resonance frequency can be determined by considering that the dimensions of the resonator are much smaller than the wavelength of interest:

$$\omega_0 = \sqrt{\frac{1}{MC}} = c\sqrt{\frac{A_n}{l_{eff}\,V_c}} \tag{14}$$

The resonance's sharpness of a HR can be quantified by its quality factor $Q$, given by:

$$Q = \frac{\omega_0 M}{R} \tag{15}$$

## 4.3. Finite Element Model

The cavity of a LPRE combustion chamber was analyzed using FEM in configurations without and with resonators. The first was modeled using 11,136 linear solid hexahedral elements, 12,510 nodes (12,093 degrees of freedom) and the second was modeled using 38,052 linear solid tetrahedral elements, 7,493 nodes (7,399 degrees of freedom). Both meshes are shown in Fig. 22. The fluid is air at 15º C. The eigenfrequencies were calculated from 0 to 2,400 Hz. Nodal pressures on the openings were assigned to zero.



(a)                                        (b)
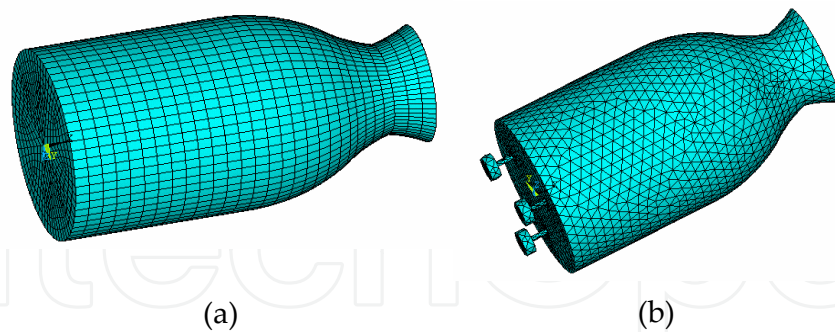
**Figure 22.** a) Cavity without resonators; b) Cavity with resonators

## 4.4. Experimental setup

Figure 23 shows the experimental setup. The mid-high frequency volume acceleration source is composed by a driver, a tube and a nozzle, where it is installed a volume acceleration sensor. This source produces a voltage signal proportional to the volume acceleration [$m^3/s^2$] variation, with a nominal frequency range of 200 up to 8,000 Hz. This source nozzle was installed in the mock-up plane surface as shown in Fig. 23.
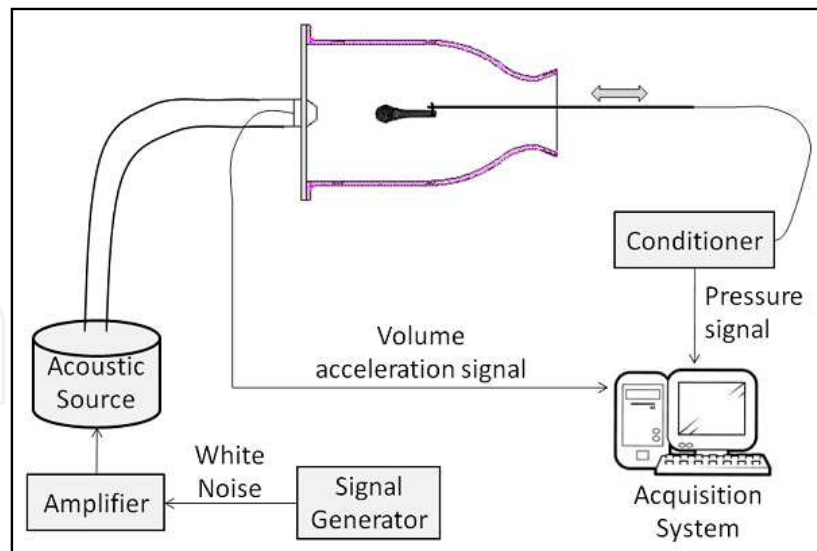
**Figure 23.** Measurement setup
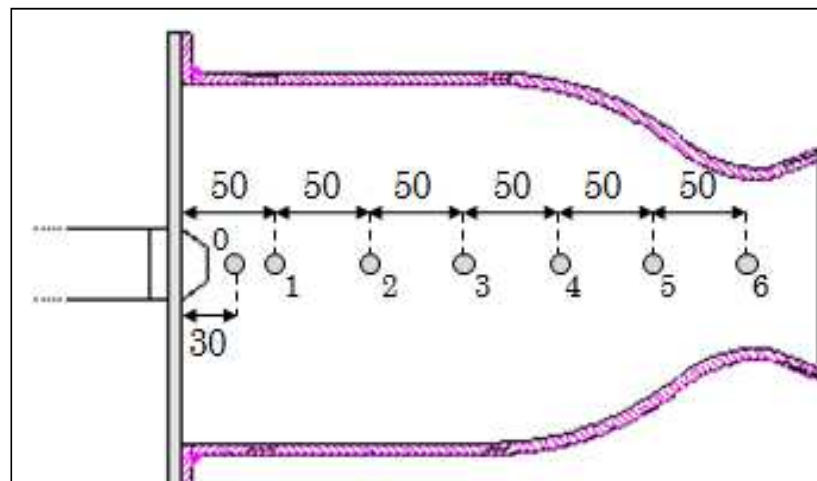


**Figure 24.** Source and microphone positions (distances in mm)

The chamber excitation was provided by a signal generator, a power amplifier and the source. The microphone was supported by a thin rod, placed in each measurement point inside the cavity. The pressure oscillations inside the cavity were captured by the microphone and registered by the data acquisition system. The volume acceleration source channel was settled as the reference channel. A white noise was used as excitation signal and the FRF were acquired at 7 points along the longitudinal axis (Fig. 24), being the point 0 the FRF driving point. The FRF were obtained by considering the volume acceleration as the excitation and the sound pressures as the responses. In order to make compatible theoretical x experimental comparisons, the volume velocity was assessed (instead of volume acceleration).

## 4.5. HR design

The objective is to tune the HR resonance as the same frequency that must be attenuated. Due to construction facility; it was chosen a cylindrical shape to develop the HR. Not only

the resonance frequency must be observed during the design process, but also several factors that influence directly the behavior of the HR:

- Resonance frequency of interest = 730 Hz (second longitudinal mode to be attenuated);
- Relation HR dimensions and wavelength $\lambda$ (must be at least 10 times smaller than $\lambda$);
- Area Ratio (AR) must be smaller than 0.16, in order to assure an end mass correction
- Quality Factor (Q): monitored to be used in future designs (compare with other HR shapes);
- Constructive factors. Define such dimensions that can be feasible constructively.

The parameters used in the design were updated considering the room temperature (28 °C) observed during the experiment:: sound speed: $c = 348.3\ m/s$; air density: $\rho = 1.1839\ kg/m^3$; air dynamic viscosity: $\mu = 1.983 \times 10^{-5}\ kg/ms$.

Considering the geometric dimensions in Eq. (14), one obtains the tuned resonance frequency as $726\ Hz$, with a quality factor of $Q = 372.8$. The acoustic parameters were calculated $M = 1019\ kg/m^4$, $C = 4.72 \times 10^{-11}\ s^2 m^4/kg$, $R = 12468\ kg/sm^4$, using the Eq. (9), (10) and (11), respectively.

Three HR were manufactured in nylon. The presented measurement methodology was repeated in order to acquire the same FRF, considering the new configuration, with the resonators.

## 4.6. Results

The identified natural frequencies are summarized in Table 6. The transversal modes frequencies were identified only numerically. Considering the first four longitudinal modes, the maximum error comparing the numerical and experimental estimation of natural frequencies was 6.6%.

Figures 25a, 25c and 25e present the three first longitudinal numerical modes.

| Mode | Experimental | Numerical | Error (%) |
|---|---|---|---|
| Longitudinal 1st | 164.50 | 170.28 | 3.51 |
| Longitudinal 2nd | 730.85 | 721.90 | 1.23 |
| Transversal 1st | - | 1126.00 | - |
| Transversal 2nd | - | 1126.00 | - |
| Longitudinal 3rd | 1272.64 | 1296.00 | 1.84 |
| Transversal 3rd | - | 1382.00 | - |
| Transversal 4th | - | 1382.00 | - |
| Longitudinal 4th | 1689.52 | 1801.00 | 6.60 |

**Table 6.** Experimental and Numerical Natural Frequencies (Hz)
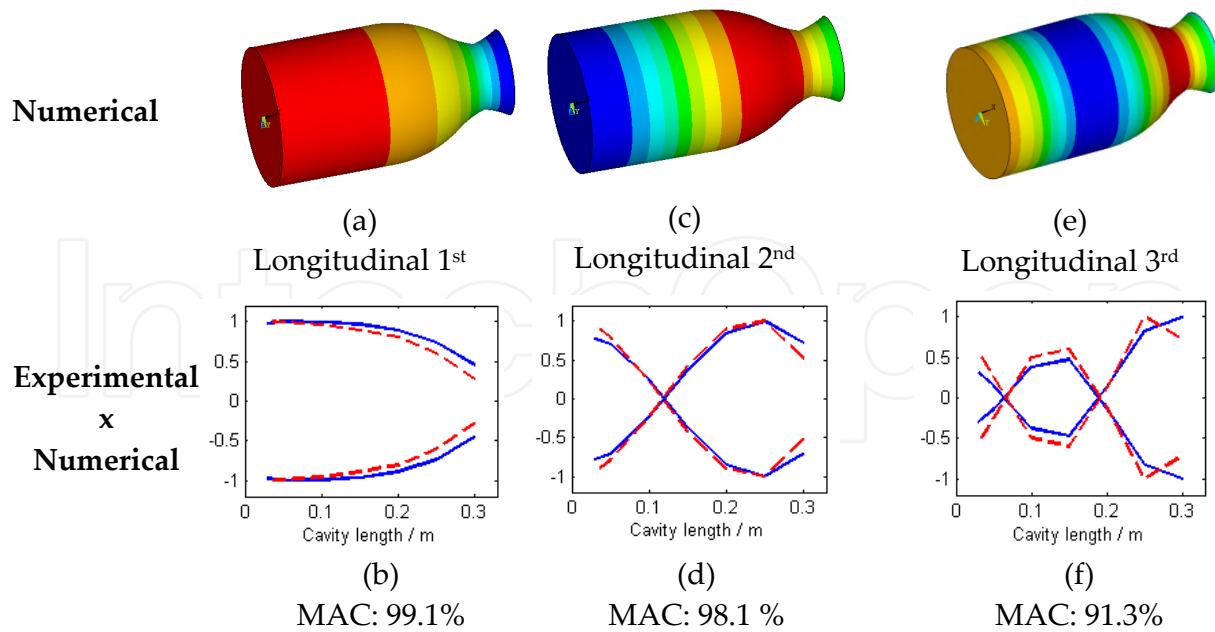
**Figure 25.** a) to f) Numerical modes and comparison between experimental (blue line) and numerical (red line) longitudinal mode shapes

Experimental versus numerical modes comparison, considering the normalized amplitude is also shown (Figs. 25b, 25d and 25f). In the numerical modes represented by the collor maps pictures (Figures 25a, 25c and 25e) the nodal regions are in green. The MAC (Eq. (7)) is also presented.

Notice in Fig. 25 that MAC values are bigger than 91% for the three first modes. For the first and second modes MAC values reach about 99%. Figures 25d and 25f show that the nodes in these modes are almost at the same point. After the introduction of the HR, the attenuation of the second mode is clearly noted in Fig. 26a, when comparing measurement results of the original cavity. At least 9 dB of attenuation can be observed in the new configuration. The FRF with and without HR are almost the same, but the second mode region (about 730 Hz), where the HR is tuned.

Figure 26 depicts the behavior of the chamber with HR. Numerical mode shapes of the configuration with HR were plotted and correlated to each part of the experimental FRF. The Fig. 26b was zoomed from the squared highlight in Fig.26a (point 1). This allows visualize the entire system behavior.

In Fig. 26 it can be noticed that mode shapes *(c)* and *(d)* have similar behavior, but different natural frequencies: it can be realized that the pressures inside all resonators vary in phase. In this case, the pressure inside the chamber remains almost unchanged. In the mode shapes *(e)* and *(f)*, the resonators act close its tuned frequency. In these modes, the whole chamber behaves as a nodal region and the pressure inside the resonators varies out of phase.

As a result of the movement of the air mass inside the neck in the four modes represented in Figs. 26, the acoustic energy on the resonators behaves as expected, reducing the energy inside the chamber.
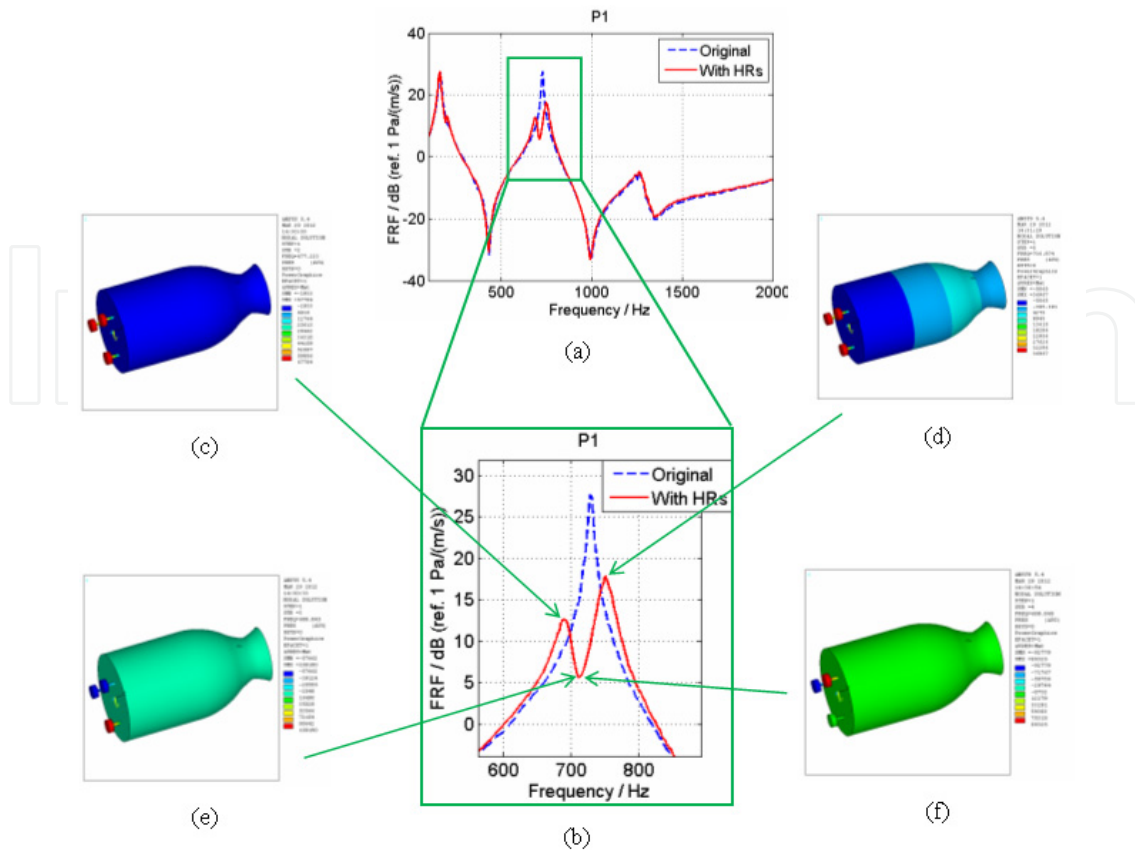
**Figure 26.** Numerical mode shapes near the resonances of the HR

## 5. Conclusions

This chapter presents three acoustic case studies applied on rocketry design.

Firstly, microphone protection devices design procedures for in-flight measurements are described. The modeling techniques using analytical and FEM numerical tools are presented as well as the validation acoustic testing procedures are presented. Good agreement among numerical and experimental results was obtained. A procedure to asses the SPL outer the launcher's structure by using the adapters' acoustic transfer functions and internal SPL measurements was also described.

Vibro-acoustic virtual prototypes were used to predict the acoustic response of a PLF cavity when excited by an ADF of 145 dB OSPL ranging from 5 to 8,000 Hz, generated at lift off.

Coupled deterministic techniques, using FEM/FEM and FEM/BEM, were applied to the fairing problem in a low-frequency band, considering accurate and efficient modeling techniques. The modal and semi-modal superposition techniques were applied to perform a FRA. In the higher frequencies, SEA coupling technique was applied to obtain the fairing acoustic responses in 1/3 octave bands.

The fairing was submitted to the lift off excitation in acoustic reverberant test and the internal acoustic pressure levels were measured. Experimental and numerical results show good agreement, except for the frequencies below 50 Hz and above 4,000 Hz.

The sensitivity analysis of acoustic blankets showed to be an effective tool for the development of the fairing NCT design. The effectiveness of a NCT considering its weight and performance can easily be evaluated using SEA, still in the development phase, when detailed subsystems are not required.

By analyzing many NCT configurations one can provide a library of performances and weights, important parameters that describe the ELV performance book. As in space industry the cost of a mission is a major issue, a trade-off between NCT weight and efficiency must be accounted. Acoustic testing in reverberant chamber may be conducted to validate the presented results and other porous-elastic materials may be investigated to complement the fairing NCT design library.

Finally, for the third case study, the use of a volumetric source in Experimental Acoustic Modal Analysis has important role in the process, once allows the accurate measurement of acoustic FRF.

The numerical model results were used as the basis for the HR design, in a first moment. In addition, numerical and experimental models were used to identify and localize, with a level of security, the node and maximum amplitude regions of each mode. The HR design seemed to be adequate, once it was verified an attenuation of 9 dB or bigger, depending of the location inside the chamber.

## Author details

Rogério Pirk[*], Carlos d´Andrade Souto and Gustavo Paulinelli Guimarães
*Institute of Aeronautics and Space (IAE) and*
*Technological Institute of Aeronautics (ITA), São José dos Campos, Brazil*

Luiz Carlos Sandoval Góes
*Technological Institute of Aeronautics (ITA), São José dos Campos, Brazil*

## 6. References

[1] Jorge P. Arenas, Ravi N. Margasahayam, 2006, Noise and Vibration of Spacecraft Structures, Ingeniare. Revista Chilena de Ingeniería, vol. 14 Nº 3, pp. 251-264

[2] Pirk, R, Sas, P., Desmet, W. and Góes, L. C. S., "Vibro-Acoustic Analysis of the Vehicle Sattelite Launcher´s (VLS) Fairing", Ph. D. Thesis, 2003, Technological Institute of Aeronautics (ITA), São José dos Campos, Brazil.

[3] Pirk, R. and Góes, L. C. S., 2006, "Acoustic Theoretical x Experimental Comparison of the Brazilian Satellite Launcher Vehicle (VLS) Fairing", Proceedings of the ISMA 2006, Leuven, Belgium.

[*] Corresponding Author

[4]  Pirk, R. and Souto, Carlos, d´A, 2009, Implementation of Acoustic Blankets to the VLS Fairing – A Sensitivity Analysis Using SEA, Proceedings of the ISMA 2008, Leuven, Belgium.

[5]  Scott, J. M., Jay, B. G., Robert, C. B., 1996, General Environmental Specification for STS and ELV – Payloads, Subsystems and Components, GEVS-SE, Rev. June 1996, NASA Goddard Space Flight Center, Maryland, 20771.

[6]  Souto and Pirk, 2009, Estimation of the external sound pressure levels generated during VLS – 1 lift off, Institute of Aeronautics and Space, Technical Report RT 001/AIE/R/2009).

[7]  Pirk et al. 2010, Alternative External Acoustic Loads Estimation of the Brazilian Satellite Launcher (VLS-1), Using In-Flight Experimental Data, International Congress on Sound and Vibration, Rio de Janeiro, Brazil

[8]  Glaese, R. M. and Anderson, E. H., 2003, "Initial Structural-Acoustic Modeling and Control Results for a Full-Scale Composite Payload Fairing for Acoustic Launch Load Alleviation".
http://www.csaengineering.com/techpapers/technicalpaperspdfs/CSA1999_Initial Structural

[9]  Weissman, K., McNelis, M. E. and Pordan, W. D., 1994, "Implementation of Acoustic Blankets in Energy Analysis Methods with Application to the Atlas Payload Fairing, Journal of the Institute of Environmental Sciences – IES, July/August 1994.

[10] Bolton, J. S., 2005, "Porous Materials for Sound Absorption and Transmission Control", Proceedings of the 2005 Congress and Exposition on Noise Control Enginnering, INTERNOISE 2005, Rio de Janeiro, Brazil.

[11] H. Defosse, M.A. Hamdi, "Vibro-acoustic study of Ariane V launcher during lift-off", Proc. of Inter-Noise 2000, vol 1, 9-14 (Nice, 2000).

[12] Culick, F.E.C. Combustion Instabilities in Liquid Rocket Engines: Fundamentals and Control. California Institute of Technology, 2002]

[13] Burnley, V.S.; Culick, F.E.C., The Influence of Combustion Noise on Acoustic Instabilities, Air Force Research Laboratory, OMB Nº 0704-0188, 1997.

[14] R. Pirk, C. d´A. Souto, D. D. Silveira and C. M. Souza, 2010, Liquid rocket combustion chamber acoustic characterization, Journal of Aerospace Technology and Management.

[15] Laudien, E. and Others 1994, Experimental Procedures Aiding the Design of Acoustic Cavities, DASA- Deutsche Aerospace AG, Liquid Rocket Engine Combustion Instability, Progress in Astronautics and Aeronautics, Chapter 14, volume 169

[16] Natanzon, M. S., 1999, Edited by Culick, F. E. C., California Institute of Technology

[17] Troclet, B., Analysis of Vibro-acoustic Response of Launchers in the Low-Frequency and High-Frequency Range, Proc. of NOVEM 2000, (Lyon, France, 2000).

[18] Khlybov, V. I. and Mak´hankov, S. A., 2009, The Preparation to Experimental Studies and Acoustic Sensors Testing Program Development, Technical Report.

[19] Kinsler, Lawrence E.; Frey, Austin R. Fundamentals of Acoustics, John Wiley & Sons, 2nd edition, 1962

[20] W. Desmet, D. Vandepitte, 2001, Finite Element Method in Acoustics, Course Graduate School in Mechanics – Advanced Acoustics, Katholieke Universiteit Leuven

[21] Coyette, J-P, Lecomte, C. & Meerbergen, K., 1997, Treatment of Random Excitations using SYSNOISE Rev. 5.3.1 – Documentation Theoretical Manual, Users Manual and Validation Manual, LMS Numerical Technologies NV.

[22] Klos, J. et al ,2003, Sound Transmission Through a Curved Honeycomb Composite Panel, AIAA Conference Paper AIAA-2003-3

[23] Desmet, W, Vandepite, D., Boundary Elements in Acoustics, Katholieke Universiteit Leuven (KUL), 2001.

[24] Lyon and DeJong, Theory and Application of Statistical Energy Analysis, Second Edition, 1995

[25] Thinh, T. Do, Vibro-acoustic Modeling Study of the Delta II 10-Foot Composite Fairing, Journal of the IEST, November/December 1999.

[26] Allard, J. F., 1993, Propagation of Sound in Porous Media – Modeling Sound Absorbing Materials, Elsevier Applied Science, London and New York.

[27] Sutton, G. P., Biblarz, O., 2001, "Rocket Propulsion Elements", New York, John Wiley & Sons.

[28] Santana Jr., A. Investigation of Passive Control Devices to Suppress Acoustic Instability in Combustion Chambers. Thesis of doctor in science. Aeronautics Institute of Technology, São José dos Campos, Brazil, 2008.

[29] Guimarães, G.P.; Pirk, R.; Souto C.A.; Góes, L.C.S. Acoustic Modal Analysis of Cylindrical-Type Cavities. Proceedings of the 8th Intern. Confer. on Structural Dynamics – EURODYN, Leuven, Belgium, 2011, p. 3160-3167.

[30] Fahy, F. Fundamentals of Engineering Acoustics. Academic Press. London, UK. 2001.